Measurement of third harmonic voltage in ferromagnet–heavy metal heterostructures

Quanzhi Zhang, Ze Yan, Aohua Ying, Jianrong Zhang, Bo Zhang, Jiangwei Cao, Mingsu Si,
Li Xi, Desheng Xue,[*] and Dezheng Yang[†]

Key Laboratory for Magnetism and Magnetic Materials of Ministry of Education,
Lanzhou University, Lanzhou 730000, China

The second harmonic voltage has been widely used to measure electrically driven spin torques in ferromagnet–heavy metal heterostructures. Based on the macrospin model, the third harmonic voltage is proposed for studying thermally driven spin torques. Our experiments clearly show that two distinct physical mechanisms dominate such thermal spin torques. The first refers to thermal expansion or contraction, which generates an effective field through the magnetoelastic effect. The second comes from the thermally reduced magnetization of the ferromagnetic layer, which modulates the magnetoresistance of the heterostructure. Our study illustrates the versatile applicability of the third harmonic voltage in investigating the nonlinear effects in ferromagnet–heavy metal heterostructures.

I. INTRODUCTION

The current-induced spin-orbit torque (SOT) [1,2] emanating from the spin Hall effect (SHE) [3–5] and/or the Rashba-Edelstein effect (REE) [6–8] facilitates efficient magnetization manipulation, such as magnetization switching [9,10], magnetization precession [11], and domain wall propagation [12,13]. The quantitative measurement of SOT is essential for estimating the efficiency of SOT-related devices. A primary technique for measuring SOT is the second harmonic voltage method, which encompasses both longitudinal and transverse configurations and is prevalently employed in ferromagnetic metal–heavy metal (FM-HM) bilayers [14–17]. Injecting an alternating current, denoted as $I(t) = I_0 \sin \omega t$, into the FM-HM heterostructure engenders an alternating spin current I_s within both the HM layer and the FM-HM interface, thereby inducing SOTs on the FM which oscillate its magnetization. Since the resistance of heterostructure $R(t)$ depends on the FM magnetization $M(t)$, the magnetization oscillation leads to resistance oscillation, expressed as $R(t) = R[M(t)] = R(M_0) + (\partial R / \partial M)(\partial M / \partial t)\delta t$, with M_0 being the equilibrium position of $M(t)$. Consequently, the total voltage $V(t) = R(t)I(t)$ incorporates a SOT-induced second harmonic component. Given that SOT devices typically necessitate a substantial current density ($\sim 10^{10}$ A/m²) [14–18], the electrically driven spin torque invariably coexists with thermal effects, thereby contributing to the thermally driven spin torques [19–23].

To quantitatively separate the thermally driven spin torque from the electrical SOT, pioneering works often employ a nonlocal lateral geometry based on the second harmonic voltage to address this issue [24]. For instance, in the FM_1/nonmanget (NM)/FM_2 lateral structure, when an alternating current $I(t)$ passes through FM_1, the resulting Joule heat generates a thermally induced spin current, contingent upon the magnetization direction of FM_1. This heat-induced spin current is injected into NM and diffuses toward FM_2, thereby inducing a voltage at the NM-FM_2 interface. As this voltage originates from the thermal spin injection, it exhibits a second harmonic voltage dependency and scales with I^2. Similarly, nonlocal magnon transport driven by electricity and heat has been distinguished in the yttrium-iron-garnet $Y_3Fe_5O_{12}$ (YIG) insulator [25], where two attached platinum (Pt) strips serve as the magnon injector and detector. Unlike the electrically driven magnons from SHE that cause the first harmonic voltage, the thermally driven magnons give rise to the second harmonic voltage, where the spin Seebeck effect (SSE) plays a role [26].

It remains a significant challenge to characterize thermally driven spin torques in the FM-HM heterostructures through local measurement. In local measurement, the alternating current passes through both the FM and HM layers, allowing for the generation of spin currents from the FM layer, the HM layer, and the FM-HM interface. This makes the contributions of harmonic voltage more complex, such as from the magnetoresistance effect due to thermal magnons [27,28], temperature-dependent saturated magnetization [29], the heat-driven magnetoelastic effect [30,31], and spin-dependent thermal transport [32–34]. Due to thermal torques-driven magnetization oscillation or thermally induced magnetization reduction, the thermally driven FM layer typically generates the third voltage in the FM-HM heterostructure. Recently, the third voltage [35,36] has been employed to quantify the SOT in antiferromagnet-HM heterostructure [31]. Notably, the third voltage is crucial in detecting the nonlinear SHE effect [37–39], where the spin current I_s is proportional to I^2. However, studies on the third harmonic voltage in the FM-HM heterostructures are still lacking.

[*]xueds@lzu.edu.cn
[†]yangdzh@lzu.edu.cn

In this work, we study the third harmonic voltage in the FM-HM heterostructures. Based on the macrospin model, we establish the angular-dependent third harmonic voltage from various mechanisms. In the experiment, two mechanisms, namely, the magnetoelastic effect and the SSE-induced magnons effect, from the angular-dependent third harmonic voltage are verified. We also confirm that the third harmonic voltage is unaffected by the spin current when the bilayer structure is inverted to counterpropagate the spin current. More interestingly, we further demonstrate the third harmonic voltage strongly depends on the magnetoelastic coefficients of the FM layers Ni, permalloy, and CoFeB. Our study establishes a foundation for SOT research in spin caloritronics and facilitates further exploration of the nonlinear spin torques in SOT devices.

II. MODEL OF THE THIRD HARMONIC VOLTAGE

When an alternating charge current is passed through the FM-HM bilayer, both the electrically and thermally driven spin torques modify the magnetization of the FM layer from its equilibrium state, changing the resistance and generating the corresponding harmonic voltage. In this section, we mainly analyze how these thermally induced spin torques modulate the magnetization, which generates the third voltages for both the longitudinal and transverse measurements. This method can also be expanded to analyze the out-of-plane or tilted magnetic configurations.

A. Spin torque–modulated magnetization

In order to simplify the macrospin model, we only consider two contributions to energy: the anisotropy energy and the Zeeman energy, and also neglect the in-plane anisotropy. As a result, the total energy of this system can be expressed as

$$E = -K_{out} \cos^2 \theta - \mathbf{M} \cdot \mathbf{H}, \tag{1}$$

where K_{out} is the effective out-of-plane anisotropy constant, $\mathbf{M}$ is the magnetization of the FM layer, θ and φ are the polar and azimuthal angles of magnetization, and $\mathbf{H}$ is the external field, that is, $\mathbf{H} = (H_x, H_y, H_z) = H(\sin \theta_H \cos \varphi_H, \sin \theta_H \sin \varphi_H, \cos \theta_H)$. We can obtain the magnetization equilibrium state (θ_0, φ_0) by solving $\frac{\partial E}{\partial \theta} = 0$ and $\frac{\partial E}{\partial \varphi} = 0$, which are

$$K_{out} \sin 2\theta_0 - M_s H \cos \theta_0 \sin \theta_H \cos(\varphi_0 - \varphi_H)$$
$$+ M_s H \sin \theta_0 \cos \theta_H = 0, \tag{2}$$

$$M_s H \sin(\varphi_0 - \varphi_H) \sin \theta_H \sin \theta_0 = 0, \tag{3}$$

where M_s is the saturated magnetization of the FM layer. When an additional effective magnetic field $\Delta \mathbf{H}$, i.e., the current-induced SOT effective field and Oersted field, exerts a torque on magnetization, it will change the equilibrium state of magnetization from (θ_0, φ_0) to $(\theta_0 + \Delta \theta, \varphi_0 + \Delta \varphi)$. Under the first-order Taylor expansion of Eqs. (2) and (3), we can easily obtain the linear response between $(\Delta \theta, \Delta \varphi)$ and $\Delta \mathbf{H}$ as

$$\begin{pmatrix} A_{11} & A_{12} \\ A_{21} & A_{22} \end{pmatrix} \begin{pmatrix} \Delta \theta \\ \Delta \varphi \end{pmatrix} = \begin{pmatrix} B_1 \\ B_2 \end{pmatrix}, \tag{4}$$

where $\mathbf{A}$ is known as the Hessian matrix with respect to the total energy E [40]. The matrix elements are

$$A_{11} = \frac{\partial^2 E}{\partial \theta^2} = 2K_{out} \cos 2\theta_0 + \mathbf{M} \cdot \mathbf{H}, \tag{5}$$

$$A_{12} = A_{21} = \frac{\partial^2 E}{\partial \theta \partial \varphi}$$
$$= M_s \cos \theta_0 (H_x \sin \varphi_0 - H_y \cos \varphi_0), \tag{6}$$

$$A_{22} = \frac{\partial^2 E}{\partial \varphi^2} = M_s (H_x \cos \varphi_0 + H_y \sin \varphi_0) \sin \theta_0. \tag{7}$$

$\mathbf{B}$ is the disturbance function with respect to $\Delta \mathbf{H}$, which reads

$$B_1 = M_s (\cos \theta_0 \cos \varphi_0 \Delta H_x + \sin \varphi_0 \cos \theta_0 \Delta H_y$$
$$- \sin \theta_0 \Delta H_z), \tag{8}$$

$$B_2 = M_s (-\sin \varphi_0 \sin \theta_0 \Delta H_x + \cos \varphi_0 \sin \theta_0 \Delta H_y). \tag{9}$$

To simplify notations, we define $H_k = 2K_{out}/M_s$. By solving Eq. (4), we can obtain the magnetization deviations $(\Delta \theta, \Delta \varphi)$ as a function of the effective magnetic field $\Delta \mathbf{H}$, which are

$$\Delta \theta = \frac{\cos \theta_0 (\Delta H_x \cos \varphi_H + \Delta H_y \sin \varphi_H) - \sin \theta_0 \Delta H_z}{-H_k \cos 2\theta_0 + H \cos(\theta_H - \theta_0)}, \tag{10}$$

$$\Delta \varphi = \frac{-\Delta H_x \sin \varphi_H + \Delta H_y \cos \varphi_H}{H \sin \theta_H}. \tag{11}$$

For an in-plane magnetized FM-HM bilayer [15,16], we have $\theta_0 = \theta_H = \pi/2$, and $\varphi_0 = \varphi_H$ during the magnetic field rotated in the x-y plane. Thus, we can simplify Eqs. (10) and (11) as follows:

$$\Delta \theta = \frac{\Delta H_z}{H_k - H}, \tag{12}$$

$$\Delta \varphi = \frac{-\Delta H_x \sin \varphi_H + \Delta H_y \cos \varphi_H}{H}. \tag{13}$$

B. The spin torque–induced harmonic voltage

The longitudinal and transverse resistances for the FM-HM bilayer can be expressed as [17,41]

$$R_{xx} = R_{AMR} \sin^2 \theta_0 \cos^2 \varphi_0 - R_{SMR} \sin^2 \theta_0 \sin^2 \varphi_0, \tag{14}$$

$$R_{xy} = R_{AHE} \cos \theta_0 + R_{PHE} \sin^2 \theta_0 \sin 2\varphi_0, \tag{15}$$

where R_{AMR}, R_{SMR}, R_{AHE}, and R_{PHE} are the coefficients of the anisotropic magnetoresistance effect, the spin Hall magnetoresistance effect, the anomalous Hall effect, and the planar Hall effect, respectively. When the magnetization is tuned by the change of spin torques from (θ_0, φ_0) to $(\theta_0 + \Delta \theta, \varphi_0 + \Delta \varphi)$, we can observe the changes of ΔR_{xx} and ΔR_{xy},

$$\Delta R_{xx} = (-R_{SMR} \sin^2 \varphi_0 + R_{AMR} \cos^2 \varphi_0) \sin 2\theta_0 \Delta \theta$$
$$- (R_{SMR} + R_{AMR}) \sin^2 \theta_0 \sin 2\varphi_0 \Delta \varphi, \tag{16}$$

$$\Delta R_{xy} = (-R_{AHE} \sin \theta_0 + R_{PHE} \sin 2\theta_0 \sin 2\varphi_0) \Delta \theta$$
$$+ 2R_{PHE} \sin^2 \theta_0 \cos 2\varphi_0 \Delta \varphi. \tag{17}$$

In the case of $\theta_0 = \pi/2$, Eqs. (16) and (17) are simplified as

$$\Delta R_{xx} = -(R_{\text{SMR}} + R_{\text{AMR}})\sin 2\varphi_0 \Delta\varphi, \tag{18}$$

$$\Delta R_{xy} = -R_{\text{AHE}}\Delta\theta + 2R_{\text{PHE}}\cos 2\varphi_0 \Delta\varphi. \tag{19}$$

C. 3ω voltage: Thermally induced magnetization orientation

In the following, we discuss the mechanism of thermally driven spin torque. When an alternating current $I(t)$ with frequency ω passes through the FM-HM bilayer, the thermally driven magnetization oscillates with the frequency of 2ω due to Joule heat. As a result, ΔR are also second voltage dependent according to Eqs. (18) and (19). This would induce third voltages arising from the product of I and ΔR.

1. Magnetoelastic effect

It is well known that Joule heat will cause lattice deformation. In our case, the metal strip has a shape anisotropy. When the strip is expanded along the longitudinal direction, it will correspondingly induce transverse contraction. Because the length of the strip is much longer than the width, such shape anisotropy will induce anisotropic strain $\Delta\epsilon = (\epsilon_{xx}, \epsilon_{yy}, 0)$. Solid heat transfer and strain analysis were conducted, following the procedure outlined by Zhang *et al.* [30]. The simulation results clearly indicate the presence of biaxial strain in the ferromagnetic Ni film. Because of the magnetoelastic energy $E_{\text{ME}} = b\epsilon_{xx}m_x^2 + b\epsilon_{yy}m_y^2$ [42] with b being the magnetoelastic coefficient, we can easily obtain the expression of the magnetoelastic effective field $\Delta\mathbf{H}_{\text{ME}} = -\partial E_{\text{ME}}/\partial\mathbf{M}$ and have

$$\Delta\mathbf{H}_{\text{ME}} = -\frac{2b}{M_{\text{S}}}(\epsilon_{xx}\cos\varphi_0, \epsilon_{yy}\sin\varphi_0, 0). \tag{20}$$

According to Eqs. (12) and (13), we can obtain the magnetization driven by $\Delta\mathbf{H}_{\text{ME}}$ as

$$\Delta\theta = 0, \tag{21}$$

$$\Delta\varphi = \frac{b(\epsilon_{xx} - \epsilon_{yy})\sin 2\varphi_H}{M_{\text{S}}H}. \tag{22}$$

Thus, we finally obtain the angular dependence of transverse and longitudinal third voltages according to Eqs. (18) and (19) with $\varphi_0 = \varphi_H$ in the x-y plane,

$$V_{xx}^{3\omega} = \frac{b(\epsilon_{xx} - \epsilon_{yy})}{4M_{\text{S}}H}(R_{\text{AMR}} + R_{\text{SMR}})I_0 \sin^2 2\varphi_H, \tag{23}$$

$$V_{xy}^{3\omega} = -\frac{b(\epsilon_{xx} - \epsilon_{yy})}{4M_{\text{S}}H}R_{\text{PHE}}I_0 \sin 4\varphi_H. \tag{24}$$

2. Thermally induced SOT effect

Here, we describe the heat-induced SOT effect in the HM-FM bilayer, where the interface of the HM-FM bilayer acts as a thermally driven spin current source. Under the presence of a temperature gradient normal to the film, magnons are generated in the FM layer due to the SSE [26,43,44], and subsequently, these magnons can be converted into spin current in HM due to angular momentum conservation. According to Bender's theory [19], thermally activated magnons in the ferromagnet can return to the interface and exert a

torque on the magnetization via magnon-magnon scattering with coherent dynamics. This effect can be interpreted as an interfacial temperature gradient that drives spin current into FM, which is then absorbed by the magnons. The spin current from SSE is injected into the FM layer and will exert a spin torque on the FM layer [19,45]. The torque can be expressed as $\mathbf{m}(\boldsymbol{\sigma}\times\mathbf{m} - \dot{\mathbf{m}})$, where $\boldsymbol{\sigma}$ is the spin accumulation in the HM layer along the interface. Since $\dot{\mathbf{m}}$ is very small and could be neglected, the thermal spin torque $\boldsymbol{\tau}_{\text{MM}}$ from magnons is damping-like and has $\mathbf{m}(\boldsymbol{\sigma}\times\mathbf{m})$. For an in-plane magnetized FM-HM system, the effective field $\Delta\mathbf{H}_{\text{MM}}$ can be expressed as

$$\Delta\mathbf{H}_{\text{MM}} = H_{\text{MM}}\boldsymbol{\sigma}\times\mathbf{m} = -H_{\text{MM}}(0, 0, \cos\varphi_0\sigma_y). \tag{25}$$

In the x-y plane, we have $\varphi_0 = \varphi_H$. According to Eqs. (12) and (13), we can obtain the magnetization modulation from the thermal spin current as

$$\Delta\theta = -\frac{H_{\text{MM}}}{H_K + H}\cos\varphi_H\sigma_y, \tag{26}$$

$$\Delta\varphi = 0. \tag{27}$$

According to Eqs. (18) and (19), we can further obtain the angular dependence of transverse and longitudinal third voltages,

$$V_{xx}^{3\omega} = 0, \tag{28}$$

$$V_{xy}^{3\omega} = \frac{1}{2}I_0\sigma_y R_{\text{AHE}}\frac{H_{\text{MM}}}{H_K + H}\cos\varphi_H. \tag{29}$$

Therefore, the third voltage generated by the thermally induced SOT only appears in the transverse direction.

D. 3ω voltage: Thermally induced magnetization reduction

Besides the modulation of magnetization from the spin torque, the magnitude change of magnetization will also generate a 3ω voltage. This is because the longitudinal and transverse resistances of magnetic materials depend on the amplitude of magnetization. Because heating increases the temperature, the saturation magnetization M_{S} will be slightly decreased [46]. This behavior can be simply described as

$$M_{\text{S}} = M_{\text{S}}^0(1 - \alpha_m I_0^2), \tag{30}$$

where M_{S}^0 is the saturation magnetization without current. α_m is the coefficient to represent the effect of current on the magnetization reduction. Therefore, we can rewrite Eqs. (14) and (15) as

$$R_{xx} = R_{\text{AMR}}\left(\frac{M_{\text{S}}}{M_{\text{S}}^0}\right)\sin^2\theta_0 \cos^2\varphi_0$$
$$- R_{\text{SMR}}\left(\frac{M_{\text{S}}}{M_{\text{S}}^0}\right)\sin^2\theta_0 \sin^2\varphi_0, \tag{31}$$

$$R_{xy} = R_{\text{AHE}}\left(\frac{M_{\text{S}}}{M_{\text{S}}^0}\right)\cos\theta_0 + R_{\text{PHE}}\left(\frac{M_{\text{S}}}{M_{\text{S}}^0}\right)\sin 2\varphi_0. \tag{32}$$

When the higher-order terms of I_0^2 in Eqs. (31) and (32) are ignored, the resistance changes as $\Delta R_{xx(xy)} \propto \Delta T \propto I_0^2$.

In our case, we again have $\theta_0 = \pi/2$ and $\varphi_0 = \varphi_H$. Then, we can obtain

$$\Delta R_{xx} = 2\alpha_m (R_{\text{SMR}} \sin^2 \varphi_H - R_{\text{AMR}} \cos^2 \varphi_H) I_0^2, \quad (33)$$

$$\Delta R_{xy} = -2\alpha_m R_{\text{PHE}} \sin 2\varphi_H I_0^2. \quad (34)$$

Therefore, we can obtain the angular dependence of $V_{xx(xy)}^{3\omega}$ caused by the amplitude change of magnetization,

$$V_{xx}^{3\omega} = \tfrac{1}{2}\alpha_m I_0^3 (R_{\text{SMR}} + R_{\text{AMR}}) \cos^2 \varphi_H, \quad (35)$$

$$V_{xy}^{3\omega} = \tfrac{1}{2}\alpha_m I_0^3 R_{\text{PHE}} \sin 2\varphi_H. \quad (36)$$

The amplitude reduction of magnetization by heating comes from two origins. One is the direct effect of temperature. The heating-induced-magnetization reduction arises from the change of the thermal equilibrium of magnetization due to the increasing temperature, and can be understood by the competition between thermal energy ($k_B T$) and exchange coupling, where k_B is Boltzmann constant and T is the temperature. It is well known that the amplitude of ferromagnetic magnetization gradually decreases as the temperature increases, and then approaches zero when the temperature is close to the Curie temperature [46]. The other comes from the thermally generated magnons in the FM layer, which represent heating-induced equilibrium magnon distribution with respect to temperature and nonequilibrium magnon distribution due to the presence of temperature gradient. Since the magnon spectrum is different from cold to hot, such nonequilibrium magnon distribution will generate magnon current in the FM layer. In the FM-HM bilayer, owing to the temperature gradient normal to the FM film, thermally magnon current can be further converted into spin current in HM due to the angular momentum conservation, and be observed via the inverse SHE [25], also known as the SSE. The generated magnons also decrease the saturation magnetization M_S. Unlike the direct temperature effect, the reduction of M_S from magnons is more sensitive to the magnetic field. As the magnetic field increases, the magnons will be significantly suppressed. As a result, the magnetization reduction at the large magnetic field will mainly originate from the direct temperature effect.

III. EXPERIMENTAL DETAILS

To check the validity of our theoretical model, we fabricate two sets of samples by magnetron sputtering. The first set is the FM-HM bilayer, where the FM layers are Ni, permalloy (Py), and CoFeB and exhibit negative, zero, and positive magnetoelastic coefficients, respectively. The second are the HM-FM bilayers that are just the inverted structures of the first set. For both sets, Pt is chosen as the HM layer with a fixed thickness $t = 5$ nm. To prevent oxidation, the FM-HM bilayers are capped by 3-nm Ta that is naturally oxidized to TaO_x. Additionally, we deposited a Ta layer as a buffer layer to promote smooth growth and improve the quality of the bilayer interface. The films are then patterned into 10-μm-wide Hall bar devices by the optical lithography technique and Ar-ion milling. The measurement configuration of harmonic voltage is shown in Fig. 1(a). We use a Keithley 6221 as the current source, where a sinusoidal current with a frequency of 133 Hz is applied to the Hall bar along the x axis. The transverse and
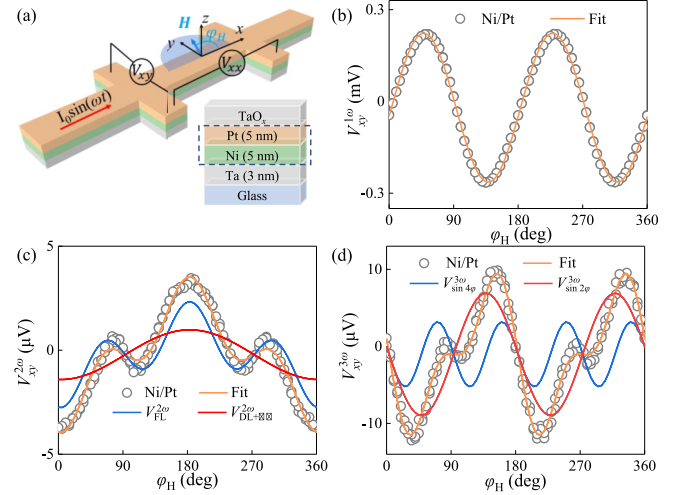
FIG. 1. (a) A schematic diagram of the transverse and longitudinal harmonic voltages measurement. The angular dependence of (b) $V_{xy}^{1\omega}$, (c) $V_{xy}^{2\omega}$, and (d) $V_{xy}^{3\omega}$ for the Ta (3 nm)/Ni (5 nm)/Pt (5 nm)/TaO_x (3 nm) sample under $H = 138$ Oe and $I_0 = 6.0$ mA.

longitudinal time-dependent voltages are collected by the data acquisition card (NI-4461) and then converted to frequency-dependent harmonic signal via Fourier transformation. The magnetic field **H** is rotated in the x-y plane. φ_H is the angle between the magnetic field **H** and the x axis. All transport measurements are carried out at room temperature.

IV. RESULTS AND DISCUSSION

A. The transverse harmonic voltages

Figures 1(b)–1(d) show the angular dependencies of first, second, and third transverse harmonic voltages for the Ta (3 nm)/Ni (5 nm)/Pt (5 nm)/TaO_x (3 nm) sample. Due to the PHE effect, $V_{xy}^{1\omega}$ in Fig. 1(b) exhibits a perfect $\sin 2\varphi_H$ angular dependence. Consistent with electrically driven magnetization oscillation [40,47,48], $V_{xy}^{2\omega}$ in Fig. 1(c) can be clearly separated into two contributions: damping-like (DL) torque and field-like (FL) torque. The DL torque and FL torque play very different roles in driving the dynamics of magnetic moments. DL torque cants the magnetic moments toward the out of plane, which induces a $\cos \varphi_H$ angular dependence, while FL torque directly rotates the magnetic moments within plane, which induces a $\cos \varphi_H \cos 2\varphi_H$ angular dependence.

Interestingly, besides the $V_{xy}^{1\omega}$ and $V_{xy}^{2\omega}$, we can also observe a significant $V_{xy}^{3\omega}$ signal in Fig. 1(d), whose amplitude is three times larger than $V_{xy}^{2\omega}$. One can easily find that the measured $V_{xy}^{3\omega}$ data are well fitted by $\sin 2\varphi_H$ and $\sin 4\varphi_H$. According to the theoretical model mentioned above, the angular components of $\sin 2\varphi_H$ and $\sin 4\varphi_H$ are respectively attributed to the thermally induced magnetization reduction of Eq. (36) and the magnetoelastic effect of Eq. (24). Moreover, the thermally induced SOT that contributes $\cos \varphi_H$ from Eq. (29) is negligible.

To further confirm $V_{xy}^{3\omega}$ originated from the thermally induced magnetization reduction and the magnetoelastic effect, we measure the angular dependence of $V_{xy}^{3\omega}$ signals under
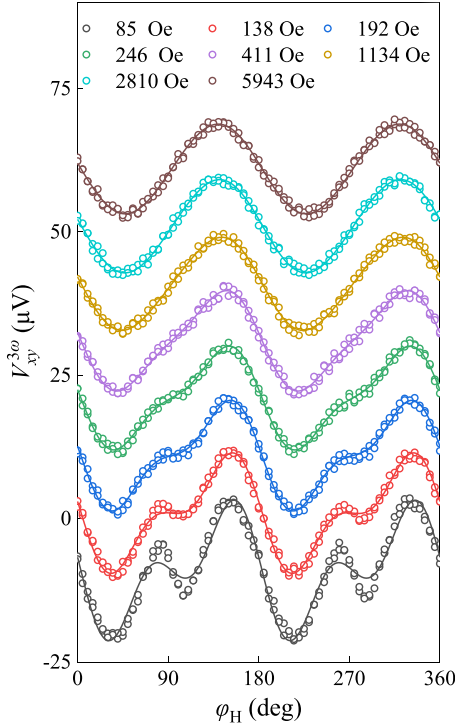
FIG. 2. The angular dependencies of $V_{xy}^{3\omega}$ under different magnetic fields with $I_0 = 6.0$ mA.

FIG. 3. (a) The magnetic field dependence of $V_{\sin 4\varphi}^{3\omega}/V_{\sin 2\varphi}^{1\omega}$, where $1/H$ is used. (Inset: The field dependence of $V_{\sin 2\varphi}^{1\omega}$, $V_{\sin 2\varphi}^{1\omega} = I_0 R_{\mathrm{PHE}}$ represents the amplitude of the first transverse voltage.) (b) The magnetic field dependence of $V_{\sin 2\varphi}^{3\omega}/V_{\sin 2\varphi}^{1\omega}$. (c) $V_{\sin 4\varphi}^{3\omega}$ and (d) $V_{\sin 2\varphi}^{3\omega}$ are proportional to I_0^3.

different magnetic fields, as shown in Fig. 2. As H increases from 85 to 5943 Oe, the angular component of $\sin 4\varphi_H$ gradually disappears, while that of $\sin 2\varphi_H$ remains nearly unchanged. We fit the experimental results with two parameters: the amplitudes of $\sin 4\varphi_H$ and $\sin 2\varphi_H$ ($V_{\sin 4\varphi}^{3\omega}$ and $V_{\sin 2\varphi}^{3\omega}$). The transverse voltage $V_{xy}^{3\omega}$ induced by magnetization reduction described in Eq. (36) not only encompasses the heat-induced magnetization reduction denoted as α_m, but is also related to R_{PHE}. As shown in the inset in Fig. 3(a), $V_{xy}^{1\omega}$ also exhibits variation in the low magnetic field range due to changes in R_{PHE}. Therefore, it would be more appropriate to directly compare $\alpha_m \propto V_{xy}^{3\omega}/V_{xy}^{1\omega}$ in Figs. 3(a) and 3(b), rather than the raw $V_{xy}^{3\omega}$. As shown in Fig. 3(a), $V_{\sin 4\varphi}^{3\omega}/V_{\sin 2\varphi}^{1\omega}$ exhibits a $1/H$ dependence for different current amplitudes I_0, and the slope gradually increases as I_0 increases. The $1/H$ dependence coincides with Eq. (24), which directly confirms the validation of our model. $V_{\sin 2\varphi}^{3\omega}/V_{\sin 2\varphi}^{1\omega}$ in Fig. 3(b) increases sharply under small magnetic fields, which arises from the thermally induced magnons effect. The thermal magnons refer to both thermally generated magnons due to SSE and the low-frequency part of the magnon spectrum during heating. As the magnons are suppressed at the larger magnetic field, $V_{\sin 2\varphi}^{3\omega}/V_{\sin 2\varphi}^{1\omega}$ becomes saturated. Owing to the larger temperature variation, increasing I_0 can induce the larger saturated value of $V_{\sin 2\varphi}^{3\omega}/V_{\sin 2\varphi}^{1\omega}$. Moreover, as shown in Figs. 3(c) and 3(d), $V_{\sin 4\varphi}^{3\omega}$ and $V_{\sin 2\varphi}^{3\omega}$ are both proportional to I_0^3, respectively, due to $\epsilon_{xx(yy)} \propto I_0^2$. However, it should be noted that the slope of $V_{\sin 4\varphi}^{3\omega}$ in Fig. 3(c) is related to the magnetic field, while the slope of $V_{\sin 2\varphi}^{3\omega}$ in Fig. 3(d) is independent of the magnetic field. The results can also be well described by Eqs. (24) and

(36). According to the fitted results, the obtained efficiency of the current-induced magnetoelastic effective fields is 0.47 Oe/mA^2 and α_m is 1.62×10^{-3}/mA^2, respectively.

B. The longitudinal harmonic voltages

In this section, we mainly discuss the angular dependencies of longitudinal harmonic voltages for Ta (3 nm)/Ni (5 nm)/Pt (5 nm)/TaO$_x$. Due to anisotropic magnetoresistance (AMR) and spin Hall magnetoresistance (SMR) effect, the angular dependence of the longitudinal first harmonic voltage $V_{xx}^{1\omega}$ is described by $\cos^2 \varphi_H$, as shown in Fig. 4(a). The angular dependence of the longitudinal second harmonic voltage $V_{xx}^{2\omega}$ in Fig. 4(b) can be separated into two angular components: $\sin 2\varphi_H \cos \varphi_H$ and $\sin \varphi_H$. The angular dependence of $\sin 2\varphi_H \cos \varphi_H$ arises from FL torque, which rotates the magnetic moments within plane. Because the longitudinal magnetoresistance effects, i.e., AMR and SMR, in the $x - y$ plane configuration are insensitive to the out-of-plane magnetic moments, we cannot detect DL torque in this case [17]. The angular component of $\sin \varphi_H$ arises from the unidirectional spin Hall magnetoresistance [28,41] and SSE. Similarly, we observe the $3w$ longitudinal voltage ($V_{xx}^{3\omega}$) in Fig. 4(c), whose amplitude is much stronger than $V_{xx}^{2\omega}$. According to our theoretical model, the measured angular dependencies of $V_{xx}^{3\omega}$ are well separated into $\cos^2 \varphi_H$ and $\sin^2 2\varphi_H$, which are contributed from the reduction of M_S of Eq. (35) and the magnetoelastic effect of Eq. (23). Moreover, the thermally induced SOT of Eq. (28) is also negligible in $V_{xx}^{3\omega}$. As shown in Fig. 4(d), we further measure the angular dependence of $V_{xx}^{3\omega}$ under different H. The angular components of $\cos^2 \varphi_H$ and the $\sin^2 2\varphi_H$ in $V_{xx}^{3\omega}$ exhibit different H dependencies. As H increases from 85 to 5943 Oe, the $\sin^2 2\varphi_H$ signal rapidly decays, while the $\cos^2 \varphi_H$ signal is
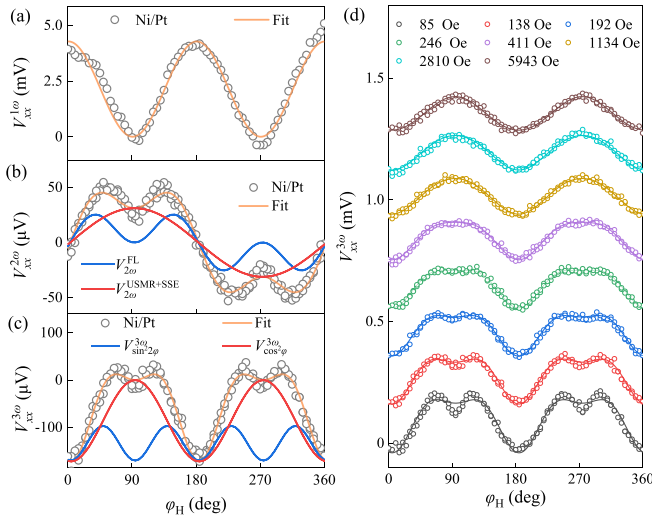
FIG. 4. The angular dependencies of (a) $V_{xx}^{1\omega}$, (b) $V_{xx}^{2\omega}$, and (c) $V_{xx}^{3\omega}$ for the Ta (3 nm)/Ni (5 nm)/Pt (5 nm)/TaO$_x$ sample under $H = 138$ Oe and $I_0 = 6.0$ mA. (d) $V_{xx}^{3\omega}$ under different magnetic fields with $I_0 = 6.0$ mA.

almost unchanged. By fitting the curves, we can obtain their amplitudes $V_{\sin^2 2\varphi}^{3\omega}$ and $V_{\cos^2 \varphi}^{3\omega}$.

For the same reason as the transverse voltage, the longitudinal voltage $V_{xx}^{3\omega}$ induced by magnetization reduction described in Eq. (35) is also related to $R_{SMR} + R_{AMR}$. As shown in the inset in Fig. 5(a), $V_{xx}^{1\omega}$ also exhibits variation in the low magnetic field range due to changes in $R_{SMR} + R_{AMR}$. Therefore, it would be more appropriate to directly compare $\alpha_m \propto V_{xx}^{3\omega}/V_{xx}^{1\omega}$ in Figs. 5(a) and 5(b), rather than the raw $V_{xx}^{3\omega}$. As shown in Figs. 5(a) and 5(b), $V_{\sin^2 2\varphi}^{3\omega}/V_{\cos^2 \varphi}^{1\omega}$ shows a $1/H$
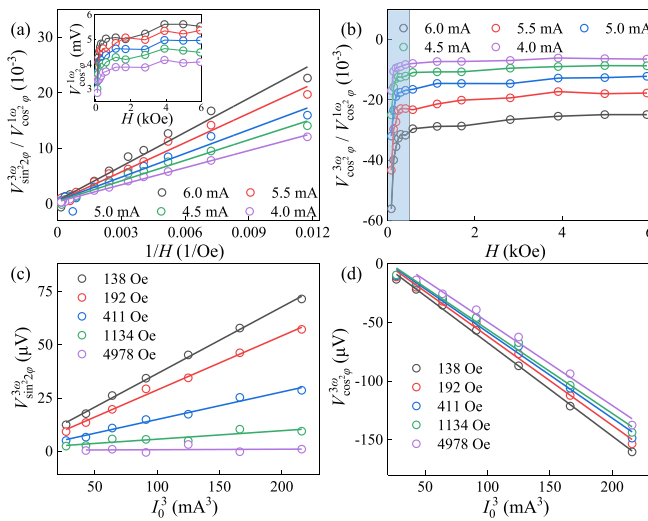
FIG. 5. (a) The magnetic field dependence of $V_{\sin^2 2\varphi}^{3\omega}/V_{\cos^2 \varphi}^{1\omega}$, where $1/H$ is used. [Inset: The field dependence of $V_{\cos^2 \varphi}^{1\omega}$, $V_{\cos^2 \varphi}^{1\omega} = I_0(R_{SMR} + R_{AMR})$ represents the the amplitude of the first longitudinal voltage.] (b) The magnetic field dependence of $V_{\cos^2 \varphi}^{3\omega}/V_{\cos^2 \varphi}^{1\omega}$. (c) $V_{\sin^2 2\varphi}^{3\omega}$ and (d) $V_{\cos^2 \varphi}^{3\omega}$ are proportional to I_0^3.

dependence, while $V_{\cos^2 \varphi}^{3\omega}/V_{\cos^2 \varphi}^{1\omega}$ varies sharply under small magnetic fields because of the thermal magnon generation, and then reaches saturation at high magnetic field. But, we also note that the thermal magnon effect in the longitudinal direction is still stronger than that in the transverse direction. This could be attributed to the fact that longitudinal detection tends to involve long-range averaging, while transverse detection is more akin to local measurements. These H dependencies for the longitudinal measurements in Figs. 5(a) and 5(b) are qualitatively consistent with those of transverse measurements in Figs. 3(a) and 3(b), indicating $V_{xx}^{3\omega}$ shares the same mechanism as $V_{xy}^{3\omega}$. Moreover, as shown in Figs. 5(c) and 5(d), $V_{\sin^2 2\varphi}^{3\omega}$ and $V_{\cos^2 \varphi}^{3\omega}$ are both proportional to I_0^3, which obey Eqs. (23) and (35), respectively. Based on fitting, the obtained efficiency of the current-induced magnetoelastic effective fields is 0.41 Oe/mA^2 and α_m is 1.62×10^{-3}/mA^2, respectively. All those values are close to those from $V_{xy}^{3\omega}$ in Figs. 3(c) and 3(d).

C. Discussion

1. Impact of the inverted structure

In order to further analyze the contributions of $V_{xy}^{3\omega}$, we fabricate Pt/Ni heterostructure that is just an inverted structure of Ni/Pt heterostructure in Fig. 1(a). Compared with $V_{xy}^{2\omega}$ in the Ni/Pt heterostructure in Fig. 1(c), Fig. 6(a) shows the angular dependence of $V_{xy}^{2\omega}$ has an opposite sign for Pt/Ni heterostructure, due to the counterpropagating spin current. However, the sign of $V_{xy}^{3\omega}$ for Pt/Ni heterostructure has not changed. These results suggest that the second and third harmonic voltages contain different mechanisms. $V_{xy}^{3\omega}$ in FM-HM heterostructure is independent of the sign of spin current, which rules out the thermally induced SOT effect in the FM-HM bilayer.

2. Evidence of the magnetoelastic effect

To further determine $V_{xy}^{3\omega}$ induced by magnetoelastic effect, we choose an FM layer with different magnetoelastic coefficients, i.e., Ni, CoFeB, and permalloy [49–51]. Because the magnetoelastic coefficient for Ni is opposite that of CoFeB, the sign of $V_{\sin 4\varphi}^{3\omega}$ for CoFeB is also reversed, as shown in Figs. 6(b) and 6(c). But the signs of $V_{\sin 2\varphi}^{3\omega}$ for Ni and CoFeB have not changed. When we further replace the FM layer with permalloy whose magnetoelastic coefficient is almost zero, $V_{\sin 4\varphi}^{3\omega}$ also becomes zero. These results indicate that $V_{\sin 4\varphi}^{3\omega}$ strongly depends on the magnetoelastic coefficient, consistent with our model in Eq. (24). Moreover, for longitudinal harmonic voltage measurement, the sign of $V_{\sin^2 2\varphi}^{3\omega}$ is also determined by the magnetoelastic coefficient of the FM layer, which further confirms the correctness of our model.

3. The 3ω voltage in a single FM film

Because the heat-induced magnetization reduction and magnetoelastic effect only related with the FM layer, it will be very interesting to further study whether the third harmonic voltage occurs in a single FM film. We fabricated Ti (3 nm)/Ni (5 nm)/TiO$_x$ samples through the same process. The Ti in the bottom layer and the top layer are used to induce smooth growth of the film and to protect it from oxidation,
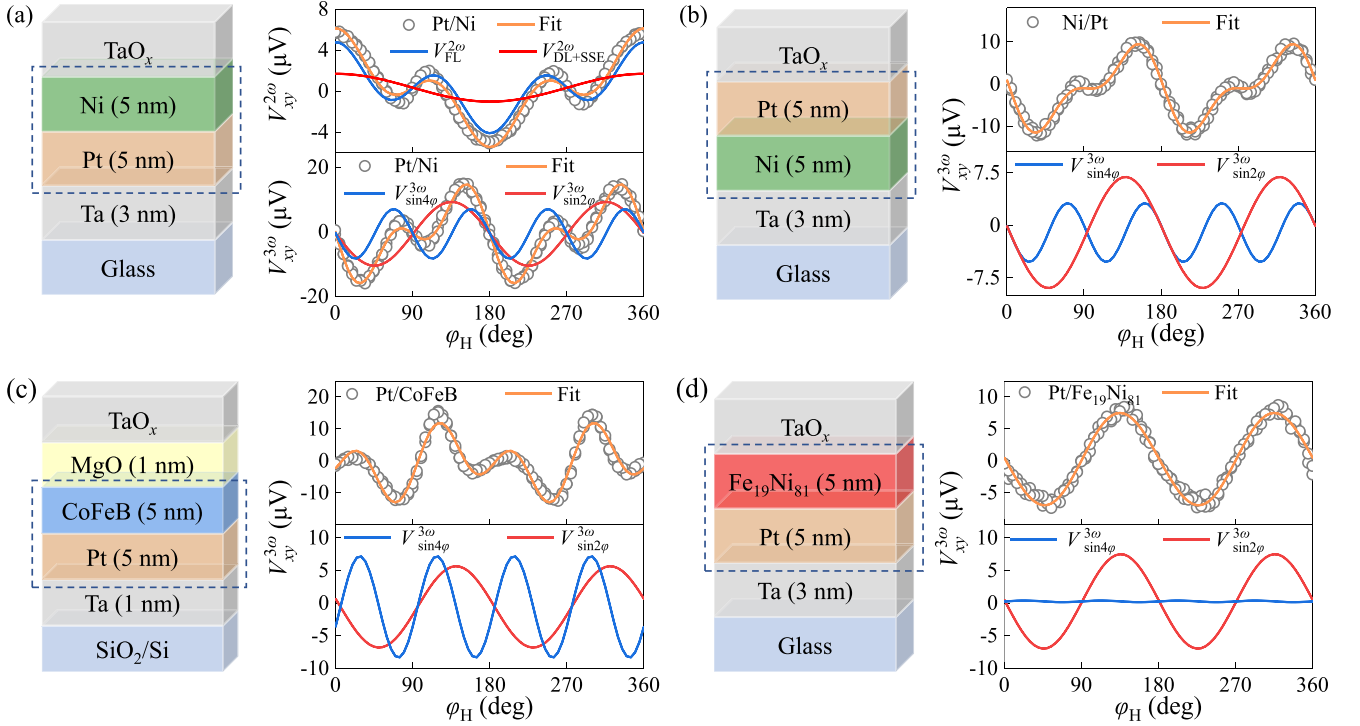
FIG. 6. (a) The angular dependencies of $V_{xy}^{2\omega}$ and $V_{xy}^{3\omega}$ for the Pt/Ni bilayer. The angular dependencies of $V_{xy}^{3\omega}$ for (b) Ni/Pt, (c) Pt/CoFeB, and (d) Pt/permalloy bilayers under $H = 138$ Oe and $I_0 = 6.0$ mA.

respectively. As shown in Figs. 7(a) and 7(c), the transverse and longitudinal second harmonic voltages also exist in the single-layer Ni due to the interface effect [52,53]. More importantly, we find that there is the third harmonic voltage in the single-layer Ni layer. As shown in Figs. 7(b) and 7(d), the third harmonic voltages for both longitudinal and transverse configurations exhibit the same angular dependencies for FM-HM bilayers, which could be attributed to the heat-induced magnetization reduction and magnetoelastic effect.
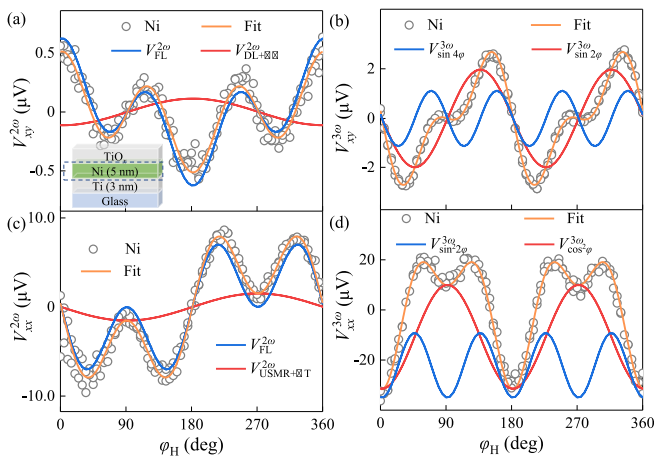
FIG. 7. The angular dependencies of the second and third harmonic voltages in transverse direction (a) $V_{xy}^{2\omega}$ and (b) $V_{xy}^{3\omega}$, and in longitudinal direction (c) $V_{xx}^{2\omega}$ and (d) $V_{xx}^{3\omega}$ for Ti (3 nm)/Ni (5 nm)/TiO$_x$ under $H = 135$ Oe and $I_0 = 2.0$ mA.

4. Analysis of nonlinear spin Hall effect

Finally, we will discuss the nonlinear spin torque in FM-HM bilayers, which can also be determined by third voltage measurement. Different from the current induced linear spin polarization such as SHE and REE, nonlinear spin polarization is theoretically predicted to exist in FM-HM bilayers, where the inversion symmetry and the time-reversal symmetry are both broken. Due to the imbalance of spin population generated by Fermi contours and Berry curves, this will result in the second-order spin Hall effect [54,55], i.e., spin current $J_s \propto E^2$. As a result, SOT arising from the nonlinear spin polarization effect can be detected by third technique. Unlike the present studies that only focus on the nonlinear spin response that occurs in high-quality single-crystal samples with central inversion symmetry, such as ThMn$_2$Si$_2$ [37], our work provides a method to further experimentally study the nonlinear spin effect in the FM-HM bilayer.

V. CONCLUSION

In summary, we theoretically and experimentally analyze various thermally driven spin torques in the FM-HM bilayer, by means of the angular dependence of the third voltage measurement. We report two striking effects: (1) the magnetoelastic effect induces $\sin 4\varphi$ and $\sin^2 2\varphi$ in transverse and longitudinal harmonic measurement, respectively, and (2) the reduction of M_S, which comes from the temperature rise and the thermal magnons, induces $\sin 2\varphi$ and $\cos^2 \varphi$ in transverse and longitudinal harmonic voltage, respectively. According to the dependence of electric current and magnetic field, as well as the measurement of inverted structure and the FM layer

with different magnetoelastic coefficients, we further verify that the harmonic voltages for longitudinal and transverse measurements contain different mechanisms, which are both explained very well by our theoretical model. Finally, we discuss the possible characterization of nonlinear spin effects in the FM-HM bilayer by using the third voltage measurement.

ACKNOWLEDGMENTS

[1] A. Manchon, J. Železný, I. M. Miron, T. Jungwirth, J. Sinova, A. Thiaville, K. Garello, and P. Gambardella, Current-induced spin-orbit torques in ferromagnetic and antiferromagnetic systems, Rev. Mod. Phys. **91**, 035004 (2019).

[2] X. Qiu, Z. Shi, W. Fan, S. Zhou, and H. Yang, Characterization and manipulation of spin orbit torque in magnetic heterostructures, Adv. Mater. **30**, 1705699 (2018).

[3] J. E. Hirsch, Spin Hall effect, Phys. Rev. Lett. **83**, 1834 (1999).

[4] J. Sinova, D. Culcer, Q. Niu, N. A. Sinitsyn, T. Jungwirth, and A. H. MacDonald, Universal intrinsic spin Hall effect, Phys. Rev. Lett. **92**, 126603 (2004).

[5] K. Ando, S. Takahashi, K. Harii, K. Sasage, J. Ieda, S. Maekawa, and E. Saitoh, Electric manipulation of spin relaxation using the spin Hall effect, Phys. Rev. Lett. **101**, 036601 (2008).

[6] H.-A. Engel, E. I. Rashba, and B. I. Halperin, Out-of-plane spin polarization from in-plane electric and magnetic fields, Phys. Rev. Lett. **98**, 036602 (2007).

[7] I. M. Miron, T. Moore, H. Szambolics, L. D. Buda-Prejbeanu, S. Auffret, B. Rodmacq, S. Pizzini, J. Vogel, M. Bonfim, A. Schuhl *et al.*, Fast current-induced domain-wall motion controlled by the Rashba effect, Nat. Mater. **10**, 419 (2011).

[8] A. Manchon, H. C. Koo, J. Nitta, S. M. Frolov, and R. A. Duine, New perspectives for Rashba spin–orbit coupling, Nat. Mater. **14**, 871 (2015).

[9] I. M. Miron, K. Garello, G. Gaudin, P.-J. Zermatten, M. V. Costache, S. Auffret, S. Bandiera, B. Rodmacq, A. Schuhl, and P. Gambardella, Perpendicular switching of a single ferromagnetic layer induced by in-plane current injection, Nature (London) **476**, 189 (2011).

[10] L. Liu, C.-F. Pai, Y. Li, H. W. Tseng, D. C. Ralph, and R. A. Buhrman, Spin-torque switching with the giant spin Hall effect of tantalum, Science **336**, 555 (2012).

[11] V.E., S. Demidov, G. Urazhdin, O. de Loubens, V. Klein, A. Cros, S. Anane, and Demokritov, Magnetization oscillations and waves driven by pure spin currents, Phys. Rep. **673**, 1 (2017).

[12] S. Emori, U. Bauer, S.-M. Ahn, E. Martinez, and G. S. D. Beach, Current-driven dynamics of chiral ferromagnetic domain walls, Nat. Mater. **12**, 611 (2013).

[13] J. Torrejon, J. Kim, J. Sinha, S. Mitani, M. Hayashi, M. Yamanouchi, and H. Ohno, Interface control of the magnetic chirality in CoFeB/MgO heterostructures with heavy-metal underlayers, Nat. Commun. **5**, 4655 (2014).

[14] J. Kim, J. Sinha, M. Hayashi, M. Yamanouchi, S. Fukami, T. Suzuki, S. Mitani, and H. Ohno, Layer thickness dependence of the current-induced effective field vector in Ta/CoFeB/MgO, Nat. Mater. **12**, 240 (2013).

[15] M. Hayashi, J. Kim, M. Yamanouchi, and H. Ohno, Quantitative characterization of the spin-orbit torque using harmonic Hall voltage measurements, Phys. Rev. B **89**, 144425 (2014).

[16] Y. Wen, J. Wu, P. Li, Q. Zhang, Y. Zhao, A. Manchon, J. Q. Xiao, and X. Zhang, Temperature dependence of spin-orbit torques in Cu-Au alloys, Phys. Rev. B **95**, 104403 (2017).

[17] B. Han, B. Wang, Z. Yan, T. Wang, D. Yang, X. Fan, Y. Wang, and J. Cao, Determination of the spin-orbit torques in ferromagnetic-heavy-metal bilayers using harmonic longitudinal voltage measurements, Phys. Rev. Appl. **13**, 014065 (2020).

[18] L. Liu, O. J. Lee, T. J. Gudmundsen, D. C. Ralph, and R. A. Buhrman, Current-induced switching of perpendicularly magnetized magnetic layers using spin torque from the spin Hall effect, Phys. Rev. Lett. **109**, 096602 (2012).

[19] S. A. Bender and Y. Tserkovnyak, Thermally driven spin torques in layered magnetic insulators, Phys. Rev. B **93**, 064418 (2016).

[20] Z. Zhang, L. Bai, X. Chen, H. Guo, X. L. Fan, D. S. Xue, D. Houssameddine, and C.-M. Hu, Observation of thermal spin-transfer torque via ferromagnetic resonance in magnetic tunnel junctions, Phys. Rev. B **94**, 064414 (2016).

[21] D. Li, S. Chen, Y. Zuo, J. Yun, B. Cui, K. Wu, X. Guo, D. Yang, J. Wang, and L. Xi, Roles of Joule heating and spin-orbit torques in the direct current induced magnetization reversal, Sci. Rep. **8**, 12959 (2018).

[22] H. Yang, H. Chen, M. Tang, S. Hu, and X. Qiu, Characterization of spin-orbit torque and thermoelectric effects via coherent magnetization rotation, Phys. Rev. B **102**, 024427 (2020).

[23] Z. Zheng, Z. Zhang, X. Feng, K. Zhang, Y. Zhang, Y. He, L. Chen, K. Lin, Y. Zhang, P. Khalili Amiri, and W. Zhao, Anomalous thermal-assisted spin–orbit torque-induced magnetization switching for energy-efficient logic-in-memory, ACS Nano **16**, 8264 (2022).

[24] A. Slachter, F. L. Bakker, J.-P. Adam, and B. J. van Wees, Thermally driven spin injection from a ferromagnet into a nonmagnetic metal, Nat. Phys. **6**, 879 (2010).

[25] L. J. Cornelissen, J. Liu, R. A. Duine, J. B. Youssef, and B. J. van Wees, Long-distance transport of magnon spin information in a magnetic insulator at room temperature, Nat. Phys. **11**, 1022 (2015).

[26] K. Uchida, S. Takahashi, K. Harii, J. Ieda, W. Koshibae, K. Ando, S. Maekawa, and E. Saitoh, Observation of the spin Seebeck effect, Nature (London) **455**, 778 (2008).

[27] M. Kobecki, A. V. Scherbakov, T. L. Linnik, S. M. Kukhtaruk, V. E. Gusev, D. P. Pattnaik, I. A. Akimov, A. W. Rushforth, A. V. Akimov, and M. Bayer, Resonant thermal energy transfer to magnons in a ferromagnetic nanolayer, Nat. Commun. **11**, 4130 (2020).

[28] C. O. Avci, J. Mendil, G. S. D. Beach, and P. Gambardella, Origins of the unidirectional spin Hall magnetoresistance in metallic bilayers, Phys. Rev. Lett. **121**, 087207 (2018).

[29] C. C. Kang, K. A. Yamauchi, J. Vlassakis, E. Sinkala, T. A. Duncombe, and A. E. Herr, Single cell–resolution western blotting, Nat. Protoc. **11**, 1508 (2016).

[30] P. Zhang, J. Finley, T. Safi, and L.-q. Liu, Quantitative study on current-induced effect in an antiferromagnet insulator/Pt bilayer film, Phys. Rev. Lett. **123**, 247206 (2019).

[31] Y. Cheng, E. Cogulu, R. D. Resnick, J. J. Michel, N. N. Statuto, A. D. Kent, and F. Yang, Third harmonic characterization of antiferromagnetic heterostructures, Nat. Commun. **13**, 3659 (2022).

[32] E. Padrón-Hernández, A. Azevedo, and S. M. Rezende, Amplification of spin waves by thermal spin-transfer torque, Phys. Rev. Lett. **107**, 197203 (2011).

[33] S. Y. Huang, W. G. Wang, S. F. Lee, J. Kwo, and C. L. Chien, Intrinsic spin-dependent thermal transport, Phys. Rev. Lett. **107**, 216604 (2011).

[34] J. Kimling, K. Nielsch, K. Rott, and G. Reiss, Field-dependent thermal conductivity and Lorenz number in Co/Cu multilayers, Phys. Rev. B **87**, 134406 (2013).

[35] D. Cahill, Thermal conductivity measurement from 30 K to 750 K: The 3ω method, Rev. Sci. Instrum. **61**, 802 (1990).

[36] C. Dames and G. Chen, 1ω, 2ω, and 3ω methods for measurements of thermal properties, Rev. Sci. Instrum. **76**, 124902 (2005).

[37] Z. Zhu, H. Liu, Y. Ge, Z. Zhang, W. Wu, C. Xiao, and S. A. Yang, Third-order charge transport in a magnetic topological semimetal, Phys. Rev. B **107**, 205120 (2023).

[38] T. Nag, S. K. Das, C. Zeng, and S. Nandy, Third-order Hall effect in the surface states of a topological insulator, Phys. Rev. B **107**, 245141 (2023).

[39] T. Kodama, N. Kikuchi, T. Chiba, S. Okamoto, S. Ohno, and S. Tomita, Observation of current-induced nonlinear spin polarization in Pt-Py bilayers, arXiv:2308.11156.

[40] W. Wang, Z. Yan, Y. Cao, C. Gao, Z. Shi, M. Si, J. Cao, L. Xi, D. Yang, and D. Xue, Generation and detection of Dresselhaus-like spin current in a single-crystal ferromagnetic metal, Adv. Funct. Mater. **32**, 2204212 (2022).

[41] C. O. Avci, K. Garello, A. Ghosh, M. Gabureac, S. F. Alvarado, and P. Gambardella, Unidirectional spin Hall magnetoresistance in ferromagnet/normal metal bilayers, Nat. Phys. **11**, 570 (2015).

[42] T. Kawada, M. Kawaguchi, T. Funato, H. Kohno, and M. Hayashi, Acoustic spin Hall effect in strong spin-orbit metals, Sci. Adv. **7**, eabd9697 (2021).

[43] J. Xiao, G. E. W. Bauer, K.-C. Uchida, E. Saitoh, and S. Maekawa, Theory of magnon-driven spin Seebeck effect, Phys. Rev. B **81**, 214418 (2010).

[44] H. Adachi, K.-i. Uchida, E. Saitoh, and S. Maekawa, Theory of the spin Seebeck effect, Rep. Prog. Phys. **76**, 036501 (2013).

[45] J.-C. Le Breton, S. Sharma, H. Saito, S. Yuasa, and R. Jansen, Thermal spin current from a ferromagnet to silicon by Seebeck spin tunnelling, Nature (London) **475**, 82 (2011).

[46] M. Yamanouchi, A. Jander, P. Dhagat, S. Ikeda, F. Matsukura, and H. Ohno, Domain structure in CoFeB thin films with perpendicular magnetic anisotropy, IEEE Magn. Lett. **2**, 3000304 (2011).

[47] S. Chen, D. Li, B. Cui, L. Xi, M. Si, D. Yang, and D. Xue, Temperature dependence of spin-orbit torques in Pt/Co/Pt multilayers, J. Phys. D: Appl. Phys. **51**, 095001 (2018).

[48] Y. Li, Y. Song, J. Zhang, Q. Yang, L. Xi, Y. Zuo, J. Zhang, M. Si, D. Xue, and D. Yang, Enhancement of spin-orbit torque in WS$_2$/Co/Pt trilayers via spin-orbit proximity effect, Phys. Rev. B **107**, L100403 (2023).

[49] D. Sander, The correlation between mechanical stress and magnetic anisotropy in ultrathin films, Rep. Prog. Phys. **62**, 809 (1999).

[50] R. Bonin, M. L. Schneider, T. J. Silva, and J. P. Nibarger, Dependence of magnetization dynamics on magnetostriction in NiFe alloys, J. Appl. Phys. **98**, 123904 (2005).

[51] D. Castilla, M. Muñoz, M. Sinusía, R. Yanes, and J. L. Prieto, Large asymmetry in the magnetoresistance loops of ferromagnetic nanostrips induced by surface acoustic waves, Sci. Rep. **11**, 8586 (2021).

[52] T. Seki, Y.-C. Lau, S. Iihama, and K. Takanashi, Spin-orbit torque in a Ni-Fe single layer, Phys. Rev. B **104**, 094430 (2021).

[53] Q. Fu, L. Liang, W. Wang, L. Yang, K. Zhou, Z. Li, C. Yan, L. Li, H. Li, and R. Liu, Observation of nontrivial spin-orbit torque in single-layer ferromagnetic metals, Phys. Rev. B **105**, 224417 (2022).

[54] C. Xiao, H. Liu, W. Wu, H. Wang, Q. Niu, and S. A. Yang, Intrinsic nonlinear electric spin generation in centrosymmetric magnets, Phys. Rev. Lett. **129**, 086602 (2022).

[55] C. Xiao, W. Wu, H. Wang, Y.-X. Huang, X. Feng, H. Liu, G.-Y. Guo, Q. Niu, and S. A. Yang, Time-reversal-even nonlinear current induced spin polarization, Phys. Rev. Lett. **130**, 166302 (2023).